Corrosion Science 163 (2020) 108276

Contents lists available at ScienceDirect

Corrosion Science

journal homepage: www.elsevier.com/locate/corsci

Multiscale corrosion-resistance mechanisms of novel ferrous alloys in dynamic aluminum melts

Gaopeng Xu, Kui Wang*, Xianping Dong, Haiyan Jiang*, Qudong Wang, Bing Ye, Wenjiang Ding

National Engineering Research Center of Light Alloy Net Forming and State Key Laboratory of Metal Matrix Composites, Shanghai Jiao Tong University, 200240, Shanghai, PR China

ARTICLE INFO

Keywords:
Al melts
Boride
Multiscale
Interfaces
Modelling

ABSTRACT

The corrosion behavior of ferrous alloys (JDF alloys and DIN1.2888) in dynamic Al melts at 750 °C has been investigated experimentally and theoretically. Results show that the compounds in JDF3 alloy can inhibit the diffusion of Al atoms in multiscales, and the borides embedded in the corrosion layer can hinder the exfoliation and dissolution of corrosion products. Based on the growth kinetics of intermetallic compounds, a numerical model has been proposed to quantitatively describe the corrosion behavior of ferrous alloys. It is demonstrated that the JFD3 alloy has two times higher corrosion resistance than FeCrB base alloy and almost four times than DIN1.2888.

1. Introduction

Aluminum alloys have been extensively applied in industry as important structural and functional materials due to their properties of lightweight, high specific strength and low cost. However, during the fabrication and processing of aluminum alloys such as melting [1], hot dip aluminizing [2,3] and die casting [4,5] etc., many metal components suffer from corrosion to different extent caused by corrosive Al and its alloy melts with high chemical activity and affinity with almost all the metals and metal oxides [6,7]. This corrosion drastically reduces their service lifetime and causes the contamination of Al melts, which in turn compromises the efficiency of aluminum processing and product quality [6,7]. Refractory metals, intermetallics and ceramics usually have desirable resistance to Al melt corrosion [8–11]. However, their high costs and difficulty in preparation greatly limit their applications. As a consequence, it is of significant necessity to develop a low-cost metal material with high corrosion resistance to satisfy industrial requirements.

Recently, Fe-B alloys attracted the attention due to their favorable corrosion resistance to Zn and Al melts [12–18]. Xing et al. [19,20] prepared the high boron cast steel by alloying and found that its corrosion resistance to Zn melts was about 5 times higher than that of 316 L. The high corrosion resistance could be largely attributed to the formation of net-like Fe_2B borides with the “protective” and “supporting” effects on the matrix. Chen et al. [21–24] investigated the corrosion behavior of Fe-Cr-Mo-B alloys in liquid Al at 750 °C, and found that the Fe-Cr-Mo-B cast steel has 5 times higher corrosion resistance than H13. They claimed that the borides, in particular the primary Cr-rich Fe_2B phases, can act as a robust barrier between the molten Al and the ferrous matrix, which effectively improved the corrosion resistance of Fe-Cr-Mo-B cast steels. However, the inherent brittleness of coarse Fe_2B phases in Fe-B alloys can adversely affect the mechanical properties and its machinability, thus severely restricting the widespread application of this material. Ma et al. [21,25–27] suggested that the addition of transition metal elements like Cr can modify the morphology of borides and therefore improve the toughness of Fe-B alloys. Nevertheless, the morphological variation of Fe_2B may not significantly improve the corrosion resistance of the Fe-B alloys in the absence of other compounds serving as the diffusion barrier to liquid Al atoms, which are likely to corrode the ferrous matrix through the gaps between the borides. Therefore, the alternative compounds acting as multiscale barriers are necessary for the further enhancement in corrosion resistance of Fe-B alloys.

Apart from the intrinsic Fe_2B and/or carbide phases in cast steel, the ceramic particles with high thermal and chemical stability are expected to be effective in inhibiting the atom diffusion without reacting with these atoms. Metal matrix composites with ceramic reinforcements are promising candidates for structural applications in wear industry primarily due to their superior toughness and wear resistance [28,29]. Additionally, previous researches [30–32] have found that the ceramic nanoparticles are able to control the phase growth by assembling onto the phase surface. The refinement of primary and eutectic phases has

* Corresponding authors.
E-mail addresses: fateratory@sjtu.edu.cn (K. Wang), jianghy@sjtu.edu.cn (H. Jiang).

https://doi.org/10.1016/j.corsci.2019.108276
Received 17 June 2019; Received in revised form 1 October 2019; Accepted 4 October 2019
Available online 15 October 2019
0010-938X/

been achieved in aluminum matrix composites. Consequently, it can be reasonably speculated that the uniformly distributed fine ceramic particles in the matrix can not only inhibit the diffusion of Al atoms through the gaps between the borides, but also can restrict the growth of coarse borides. In this case, the number density of borides can be increased in the matrix as well as the contact area between borides and Al atoms, leading to the improvement in the corrosion resistance and toughness of the Fe-B alloys.

A number of studies [18,21,33–35] were focused on the static corrosion while the dynamic corrosion gained less attention. In addition, the effect of the morphology and distribution of borides on the corrosion resistance of ferrous alloys are not fully understood, especially from the aspects of diffusion, exfoliation and dissolution. Hence, it is vital to in-depth investigate their effects on the diffusion inhibition of Al atoms, the growth restriction of intermetallic compounds (IMCs) and the dissolution hindrance of corrosion products.

In this work, novel Fe-B alloys containing multiscale compounds, named as JDF alloys, have been in-situ synthesized, which are expected to inhibit the diffusion of Al atoms in multiscales. The dynamic aluminum melt corrosion tests were performed on the JDF alloys and DIN1.2888 alloys, and the microstructure characterization of reaction layers and interfaces was conducted to unveil the effects of multiscale compounds on the corrosion resistance of ferrous alloys in dynamic Al melts. An analytical model was established to quantitatively describe the corrosion behavior of JDF alloys, based on which a multiscale corrosion-resistance mechanism was proposed to further elucidate the corrosion behavior of ferrous alloys in Al melts.

2. Materials and methods

2.1. Alloy preparation

In this work, the novel JDF alloys were melted in a 10 kg-capacity medium frequency induction furnace with the charge materials of pure iron, pure chromium, pure titanium, pure nickel, Fe-18 wt.% B, Fe-75 wt.% Si and graphite. Argon gas was introduced into the furnace for atmosphere protection. The melt was then poured into a permanent mould at 1500 ± 5 °C, and the cylindrical ingots with dimensions of Ø150 × 200 mm were obtained. For comparison, DIN1.2888 usually applied on die casting machines was used as a reference. The chemical compositions of the JDF alloys were analyzed using inductively couple plasma atomic emission spectroscopy (ICP-AES) and listed in Table 1.

2.2. Dynamic aluminum melt corrosion test

Specimens with the dimension of 70 × 10 × 5 mm^3 were cut from the center of the ingots by wire-electrode cutting, and the surfaces of specimens were polished to a mirror-like finish, ultrasonically cleaned, dried and then sized with a vernier caliper for the dynamic aluminum melt corrosion test. As shown in Fig. 1, specimens were tested in the 750 °C Al melts at a rotation speed of 60 r min^{-1} for different lengths of time, taken out, and then cooled in air. To quantitatively analyze the corrosion depth, the thicknesses of the sample matrix and IMC layers formed by the interfacial reaction were measured at each cross-section as illustrated in Fig. 1, and the thickness loss of the sample matrix (Δx) is given by

$$x = \frac{x_0 \quad x}{2} \tag{1}$$

where x_0 (μm) and x (μm) are the thickness of the sample before and after corrosion test, respectively.

2.3. Materials characterization

Samples were sectioned along the direction perpendicular to the corrosion surface, grounded with sandpaper, polished, and then etched with 4% Nitric acid alcohol solution. The microstructure of each immersed sample was observed by scanning electron microscopy (SEM; MIRA 3, Czech) coupled with the Aztec X-MaxN80 (EDS). The phase identification and distribution were analyzed using electron backscattered diffraction (Aztec Nordlys Max3 EBSD). The phase analysis of reaction products was performed using X-ray diffractometer (XRD; Smart Lab, Japan). The TEM analysis was carried out using Transmission electron microscopy (TEM; Jeol-2100 F) on the TEM foils prepared using the focused ion beam system (FIB; GAIA3).

3. Experimental results

3.1. As-cast microstructure

Fig. 2 is the XRD analysis of JDF alloys. According to the XRD results, the microstructure of JDF1 alloy is mainly composed of ferrite, M_2B-type borides (M represents both Fe and Cr) and carbides. With the addition of Ti element, TiC and TiB_2 phases can be observed in the matrix of JDF2 alloy. As the Ti content is further increased, the intensity of the diffraction peaks of TiC and TiB_2 phases is increased until 1.4 wt.% addition and then decreased.

The as-cast microstructure of JDF alloys containing various Ti contents are shown in Fig. 3. As shown in Fig. 3a, the typical microstructure of the JDF1 alloy is characterized by the coarse platelet-like primary borides and the acicular eutectic structure of the boride phase and ferrite. With increasing the Ti content from 0.7 to 1.4 wt.%, the size and aspect ratio of the primary boride are reduced, and its morphology varies from the platelet-like to block-like structure. Besides, the increment in Ti content also leads to a morphological transition of eutectic boride from coarse, continuous needle-like to fine, dispersed rod-like structure. Also notable is that the number of ceramic particles (dark spots in the matrix) is increased with the Ti content. However, when the Ti content reaches up to 2 wt.%, the ceramic particles tend to agglomerate and a number of elongated strip-like primary borides exist in the matrix again as shown in Fig. 3d. By comparison, it can be seen that the JDF3 alloy has the most refined and homogeneous microstructure.

Fig. 4a is the SEM micrograph of the JDF3 alloy. The element mapping analysis was performed on the selected area indicated by the red box in the Fig. 4a. In combination with the EDS (Table 2) and the EBSD mapping (Fig. 4b) results, it can be confirmed that both the primary borides and eutectic borides are Cr-rich Fe_2B phases. In addition, the ceramic particles in the matrix are TiC and TiB_2. These micron-sized

Table 1
Chemical compositions of the alloys.

Alloy	Main Chemical Compositions (wt.%)										
	C	B	Si	Cr	Ti	Ni	Mo	W	Co	V	Fe
JDF1	0.32	3.52	2.12	12.17	–	0.50	–	–	–	–	Bal.
JDF2	0.34	3.68	1.96	12.05	0.67	0.52	–	–	–	–	Bal.
JDF3	0.33	3.76	2.07	12.34	1.35	0.51	–	–	–	–	Bal.
JDF4	0.35	3.83	1.91	12.12	1.96	0.48	–	–	–	–	Bal.
DIN1.2888	0.25	–	0.23	9.31	–	–	2.76	5.58	10.24	0.57	Bal.

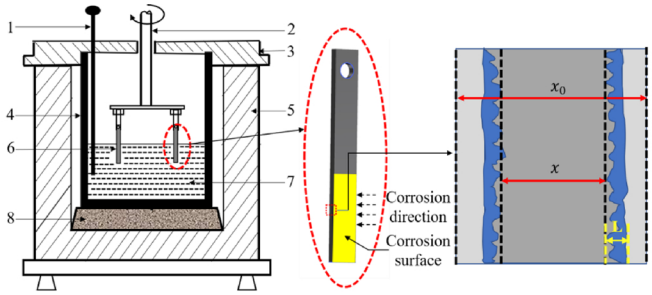

1- Thermocouple; 2- Sample holder; 3- Insulation cover; 4- Crucible; 5- Resistance furnace; 6- Sample; 7- Al melts; 8- Refractory brick

Fig. 1. Schematic of experimental set-up used for the dynamic corrosion test and the measurement of the matrix thickness loss and IMC layer thickness. 1- Thermocouple; 2- Sample holder; 3- Insulation cover; 4- Crucible; 5- Resistance furnace; 6- Sample; 7- Al melts; 8- Refractory brick.

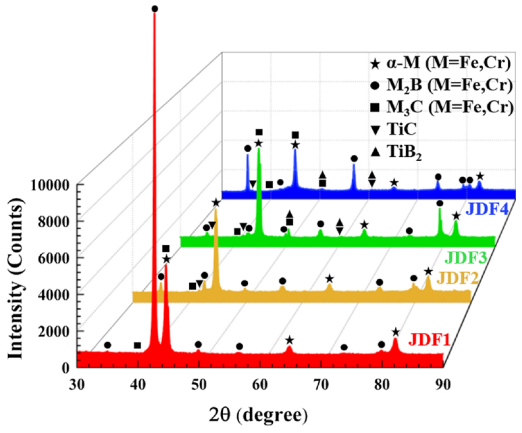

Fig. 2. X-ray diffraction patterns of JDF alloys.

ceramic particles dispersed in the matrix can not only provide the strengthening effect on the matrix, but also improve the wear resistance of the alloy. The inset in Fig. 4a is the magnified view of Fig. 4a showing the presence of a large quantity of nanoparticles (NPs) in the matrix, which are further analyzed by TEM.

Fig. 5a is the SEM micrograph of a primary Cr-rich Fe_2B in the JDF3 alloy. At the interface between primary Cr-rich Fe_2B and matrix shown in Fig. 5b, a large number of NPs are agglomerated together and accumulate closely on the surface of the primary Cr-rich Fe_2B. These NPs covering the surface of the primary Cr-rich Fe_2B phase manage to form a uniform and compact NP-layer, which can be effective in inhibiting the diffusion of the solute atoms onto the surface of the growing primary Cr-rich Fe_2B phase, restricting its growth and inducing its refinement. Furthermore, the TEM observation in Fig. 5c indicates that many NPs are also distributed along the phase boundary of the eutectic Cr-rich Fe_2B phase. Likewise, these NPs form a NP-layer coating the surface of eutectic Cr-rich Fe_2B phase. Fig. 5d is the High-resolution transmission electron microscope (HRTEM) analysis of the interface between an interphase nanoparticle and the eutectic Cr-rich Fe_2B, from which it is visible that there exists a specific crystallographic orientation between the nanoparticle and the eutectic Cr-rich Fe_2B. Based on the crystallographic information provided in Fig. 5e, the nanoparticle is likely to be Fe_3C. Therefore, the obtained orientation relationship is $(211)_{M_2B}$ 9° from $(112)_{Fe_3C}$, $[142]_{M_2B}//[311]_{Fe_3C}$. The smooth and semi-coherent interface can produce a strong interfacial bonding and thus lead to the enhanced growth-restriction effect induced by NPs.

Fig. 6 shows the bright-field TEM images of NPs distributed in the matrix of JDF3 alloy. The nanoparticle in Fig. 6a exhibits a short rod-like morphology, whose average size is ~150 nm in diameter. According to the selected area electron diffraction (SAED) in Fig. 6c, the nanoparticle in Fig. 6a is Fe_3C. Fig. 6b shows the interface between the Fe_3C and the matrix. It is obvious that the Fe_3C has a completely coherent

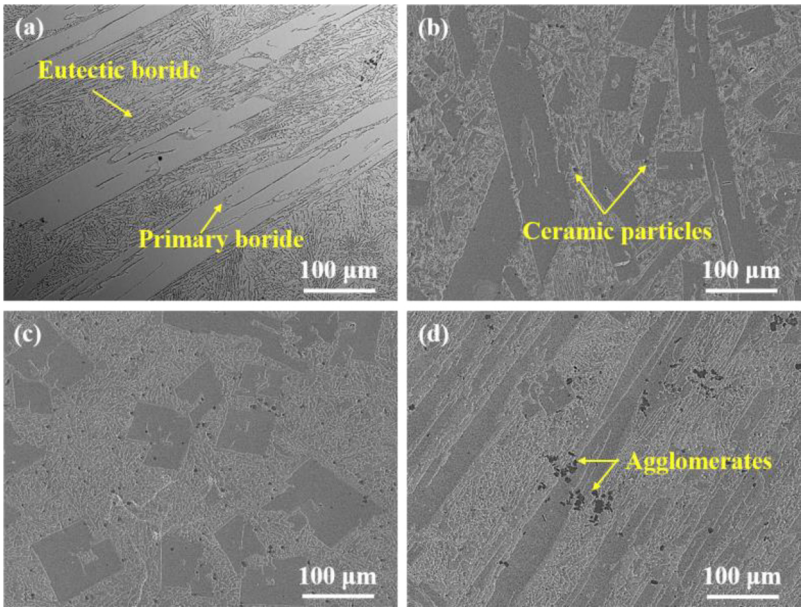

Fig. 3. SEM micrographs of JDF alloys: (a) 0 wt.% Ti; (b) 0.7 wt.% Ti; (c) 1.4 wt.% Ti; (d) 2.0 wt.% Ti.

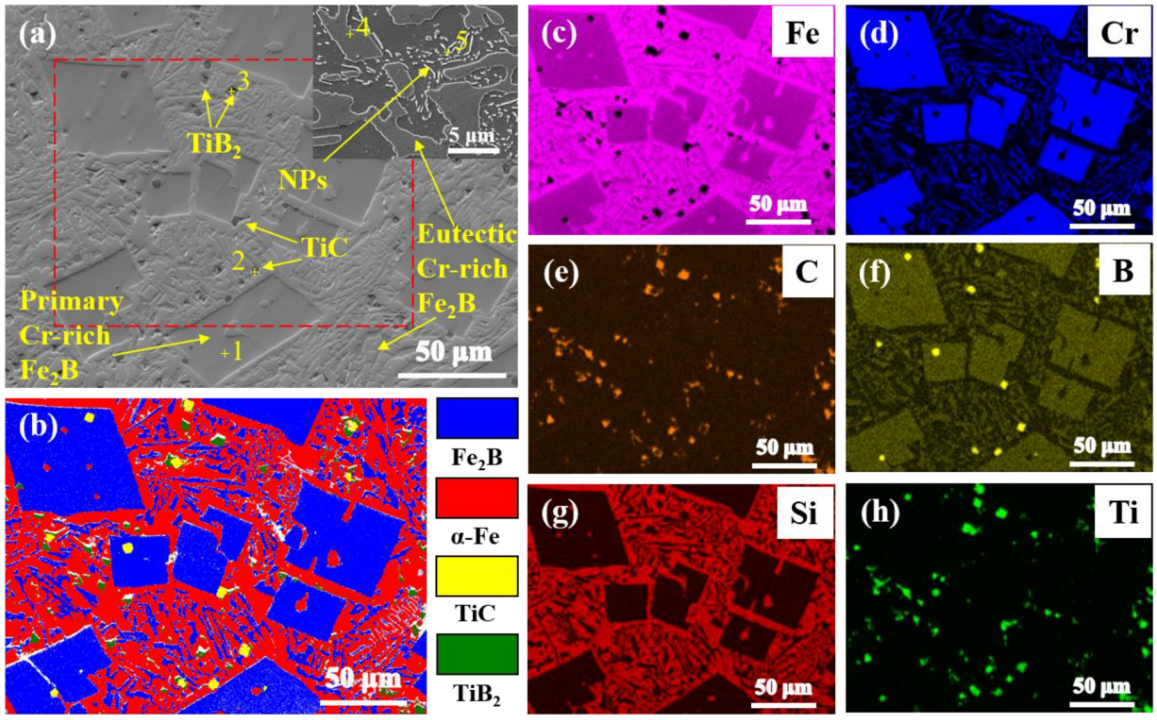

Fig. 4. Microstructure of the JDF3 alloy: (a) SEM micrograph; (b) phase distribution mapping; (c) Fe; (d) Cr; (e) C; (f)B; (g) Si; (h) Ti.

Table 2
Chemical compositions at the marked locations in Fig. 4a.

Location	Fe	Cr	EDS results (wt.%)				
			B	Ti	C	Si	Phase Compositions
1	60.27	28.76	10.97	–	–	–	$(Fe,Cr)_2B$
2	–	–	–	79.11	20.89	–	TiC
3	–	–	31.34	68.66	–	–	TiB_2
4	67.05	25.04	7.91	–	–	–	$(Fe,Cr)_2B$
5	82.08	5.50	–	–	8.61	3.81	$(Fe,Cr)_3C$

interface with the matrix, and the orientation relationship between them can be obtained as $(211)_{Fe_3C}//(101)_{Fe}$, $[142]_{Fe_3C}//[111]_{Fe}$. Fig. 6d shows that a large quantity of NPs with the size ranging from 10 to 30 nm are uniformly distributed in the matrix. The SAEDs in Fig. 6f shows that these NPs are TiB_2 nanoparticles with the HCP (hexagonal closed-packed) crystal structure. Fig. 6e gives the HRTEM analysis of the interface between a TiB_2 nanoparticle and the matrix. It is shown that the interface between them is smooth and coherent, where no intermetallic compound can be observed, and a specific orientation relationship can be achieved as $(10\bar{1}0)_{TiB_2}//(011)_{Fe}$, $[0001]_{TiB_2}//[\bar{1}11]_{Fe}$. The coherency of the interface gives a strong interfacial bonding strength between the TiB_2 and the matrix.

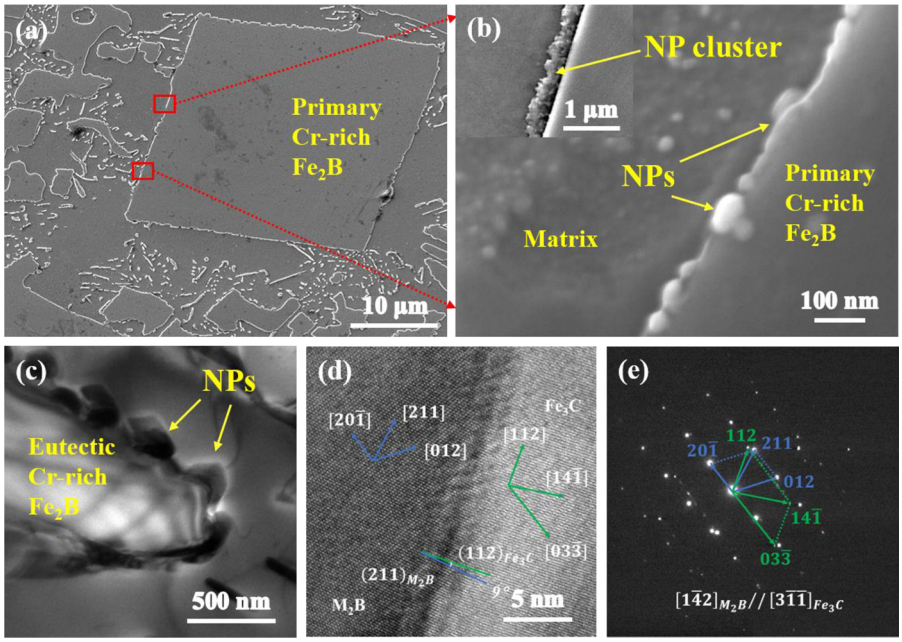

Fig. 5. (a) SEM micrograph of a primary Cr-rich Fe_2B in JDF3 alloy; (b) SEM micrograph showing the NP distribution along the phase interface of the primary Cr-rich Fe_2B; (c) TEM bright-field image of an eutectic Cr-rich Fe_2B in JDF3 alloy; (d) HRTEM image of the interface between a NP and the eutectic Cr-rich Fe_2B; (e) SAED of the interface in Fig. 5d.

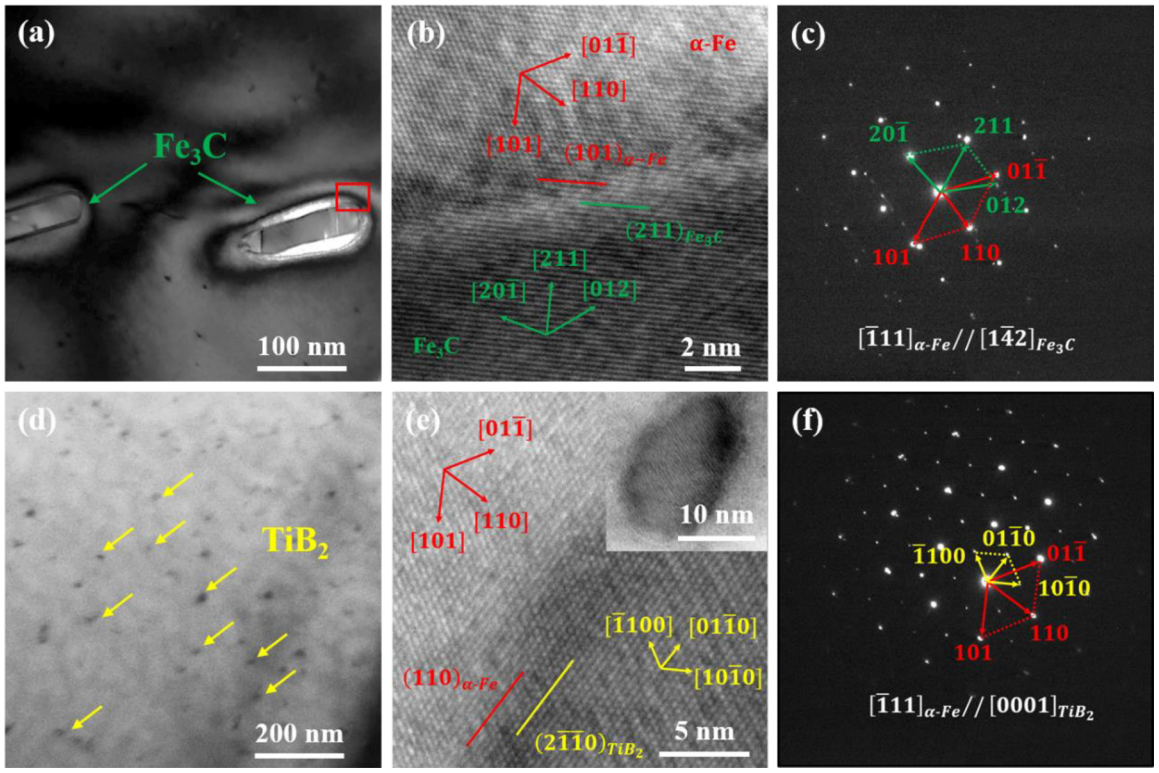

Fig. 6. (a) Bright-field TEM image of Fe_3C in JDF3 alloy; (b) HRTEM image of the interface between Fe_3C and matrix; (c) SAED of Fe_3C; (d) Bright-field TEM images of TiB_2 distributed in the matrix of JDF3 alloy; (e) HRTEM image of the interface between TiB_2 and matrix; (f) SAED of TiB_2.

3.2. Dynamic aluminum melt corrosion tests

Fig. 7 shows the corrosion depth (corrosion thickness loss) and corrosion rate as functions of corrosion time for the JDF alloys with various Ti contents and DIN1.2888 in dynamic Al melts. As the corrosion time increases, the thickness loss of the alloy is gradually increased (Fig. 7a), while the corrosion rate is gradually reduced and tends to be stable (Fig. 7b). It is demonstrated that the corrosion rates of JDF alloys are much lower than that of DIN1.2888. Therefore, it can be concluded that JDF alloys can exhibit the outstanding corrosion resistance in the dynamic Al melts. Among them, the JDF3 alloy has two times higher corrosion resistance than FeCrB base alloy and almost four times than DIN1.2888.

The interfacial morphology of DIN1.2888 corroded in Al melts at 1023 K (750 °C) for 0.5 h is shown in Fig. 8a. The interface exhibits a typical three-layer structure that consists of the left DIN1.2888 matrix, the intermediate IMC layer and the right solidified aluminum layer. The element mapping analysis was focused on the red box in Fig. 8a. Results show that the intermediate IMC layer has a bilayer structure. The layer adjacent to DIN1.2888 matrix is a transition layer which occupies the most part of IMC layer, forming an irregular tongue-shaped interface with the matrix. The tip of the tongue grows preferentially towards the matrix. Base on the EDS results (Table 3), the transition layer is composed of Fe_2Al_5 phases. Heumann et al. [36] suggested that Fe_2Al_5 grew into the matrix in a specific direction caused by the difference in the diffusion coefficients of Fe and Al. The crystal lattice of Fe_2Al_5 is

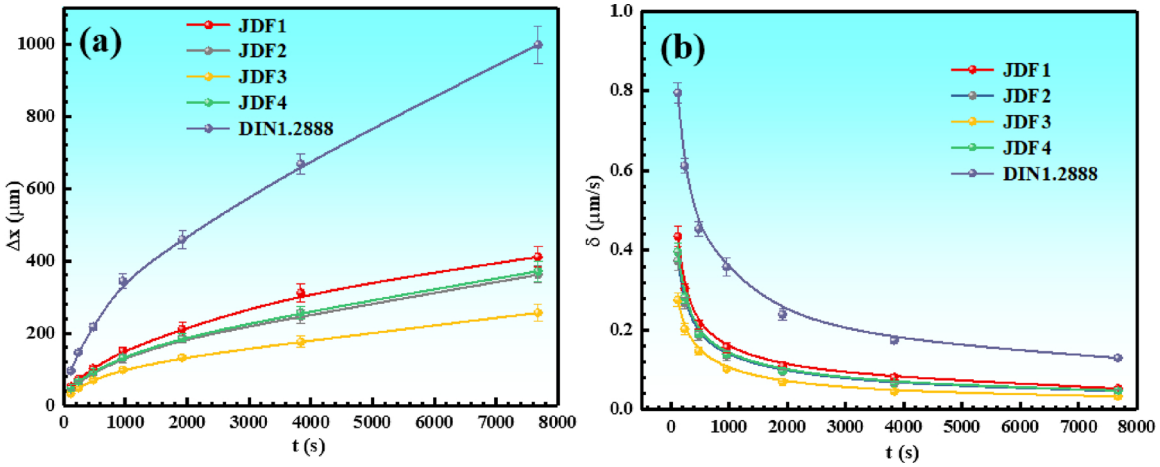

Fig. 7. Curves of corrosion depth and corrosion rate versus time during the dynamic corrosion at 1023 k (750 °C): (a) corrosion depth vs. corrosion time; (b) corrosion rate vs. corrosion time.

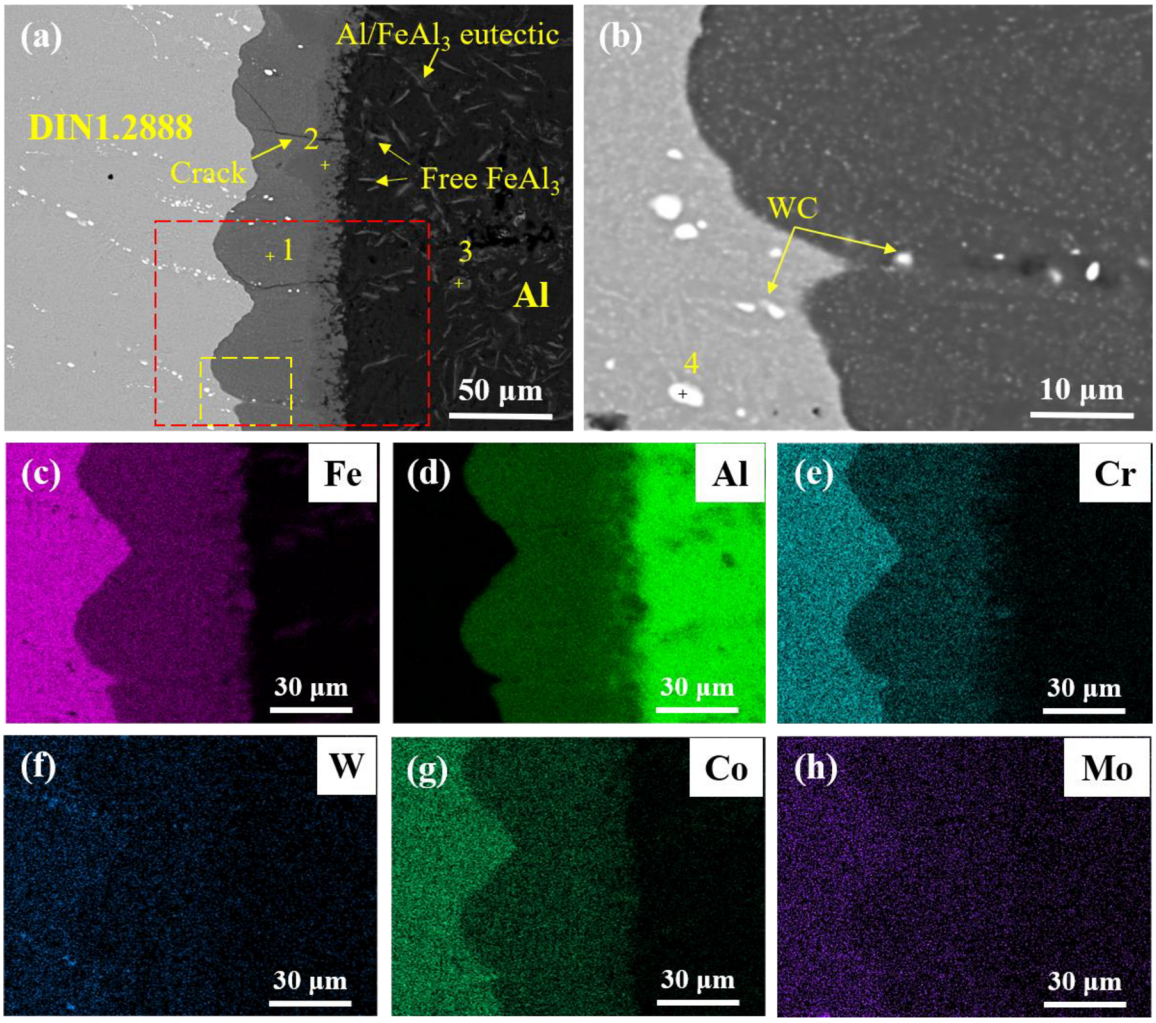

Fig. 8. SEM images and EDS analysis of the corrosion interface formed in DIN1.2888 after 0.5 h in the dynamic Al melts at 1023 K (750 °C): (a) SEM micrograph; (b) magnification image; (c) Fe; (d) Al; (e) Cr; (f)W; (g) Co; (h) Mo.

orthogonal structure, and there is a high vacancy concentration in the c-axis direction, which allows Al atoms to diffuse rapidly along the c-axis direction to the interface front, resulting in the preferential growth of Fe_2Al_5 along the c-axis direction and thus the formation of a tongue-shaped morphology [37]. Moreover, the layer adjacent to the aluminum layer is composed of $FeAl_3$ formed by the reaction diffusion and smaller than the Fe_2Al_5 layer in thickness based on the EDS results (Table 3). Several micro-cracks present in the corrosion layer can provide fast diffusion channels for the Al atoms into the matrix and accelerate the interfacial reactions, leading to the exfoliation of the interfacial layer.

At the interface between $FeAl_3$ and aluminum layer, a large number of broken particles are found to adhere to $FeAl_3$, and many strips are even freely distributed in the aluminum layer. The chemical composition of these phases is identical to that of $FeAl_3$. In fact, the formation of these $FeAl_3$ results not only from the reaction diffusion but also from the precipitation of the IMCs, while that of free $FeAl_3$ is only controlled by the precipitation process [34]. In addition, the flocculent eutectic structures are found in the solidified aluminum layer, as shown in Fig. 8a.

The interfacial morphology of JDF3 corroded in dynamic Al melts at 1023 K (750 °C) for 0.5 h is shown in Fig. 9a. The addition of B element results in the formation of a large amount of eutectic Cr-rich Fe_2B with a skeleton-like structure in the matrix. Because the Cr-rich Fe_2B has poor wettability with Al melts and reacts hardly with Al melts [22], it can greatly inhibit the diffusion of Al atoms and improve the corrosion resistance. In addition, the micron-sized ceramic particles (TiC and TiB_2) dispersed in the matrix are completely non-wetting with the Al melts and can completely block the diffusion of Al atoms. The corrosion interface of JDF3 is also a typical three-layer structure that consists of the underlying metal matrix, the intermediate IMC layer and the upper

Table 3
Chemical compositions at the marked locations in Fig. 8a.

Location	Al	Fe	C	EDS results (wt.%)		V	Mo	W	Phase Compositions
				Cr	Co				
1	50.84	36.50	3.60	4.26	3.65	0.14	–	1.01	Fe_2Al_5
2	58.43	31.89	4.65	2.33	2.70	–	–	–	$FeAl_3$
3	64.64	28.05	6.35	0.21	0.75	–	–	–	Free $FeAl_3$
4	–	32.81	20.54	7.12	3.04	1.13	6.28	29.62	WC

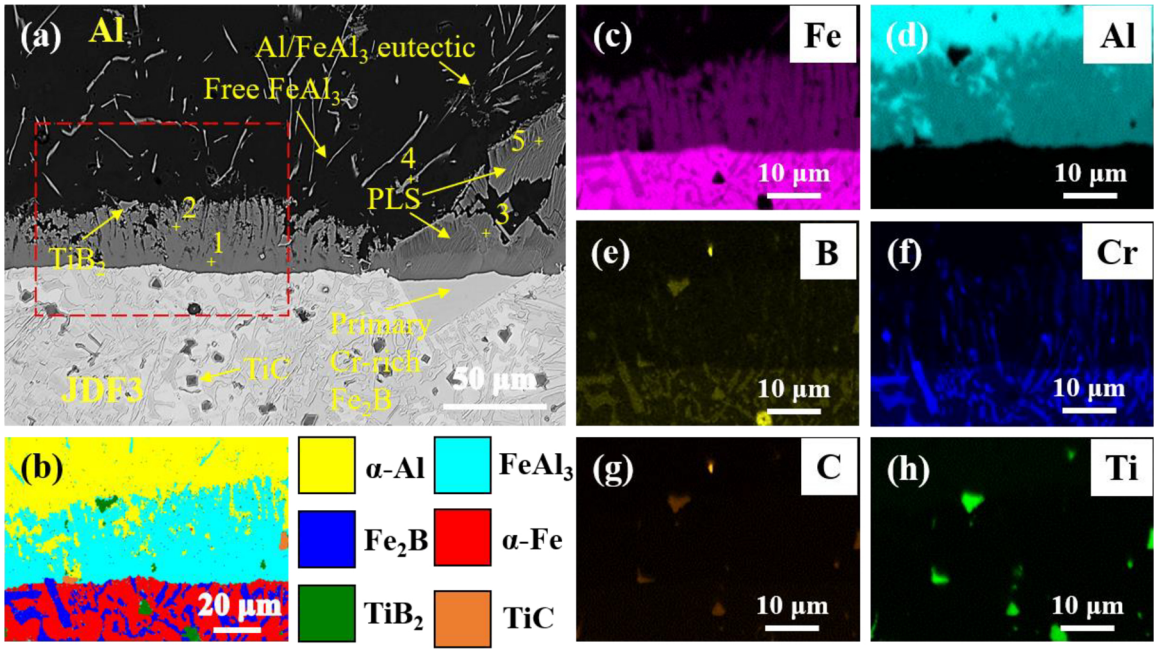

Fig. 9. SEM images, EDS and EBSD analysis of the corrosion interface formed in JDF3 alloy after 0.5 h in the dynamic Al melts at 1023 K (750 °C): (a) SEM micrograph; (b) the phase distribution map showing the different phases present in the corrosion interface; (c) Fe; (d) Al; (e) B; (f) Cr; (g) C; (h) Ti.

aluminum layer, but the layer thickness of the corrosion layer is smaller than that of DIN 1.2888. Unlike the DIN1.2888, the JDF3 alloy exhibits a uniform and regular interface between the matrix and the IMC layer. The elements mapping and EBSD analysis (Fig. 9b) was performed on the local area at the interface, and the selected area is indicated by the red box in the Fig. 9a. Results show that there is only a single $FeAl_3$ layer in the intermediate corrosion layer. Interestingly, according to the EDS element mappings of B and Cr (Fig. 9e and f), the borides are found in the corrosion layer. These borides are rooted in the matrix at one end and embedded in the IMC layer at the other end. Therefore, it can be implied that the presence of borides can result in the strengthening of the corrosion layer and the increased bonding strength between the matrix and the IMCs, which hinders the exfoliation and dissolution of corrosion products and improves the corrosion resistance of the JDF3 alloy to Al melts. Combined with EDS analysis and lite rature [22,23,38–40], these IMCs embedded in the IMC layer may be Cr-Al-B IMCs formed by the reaction of eutectic Cr-rich Fe_2 B with Al melt. Besides, it is also found that the coarse primary Cr-rich Fe $_2$ B is corroded by the Al melts, and the IMC with special periodic layered structures (PLSs) was formed in the corrosion layer [22,23,38–40]. When the diffused Al melts contact with the boride, as the (Cr, Fe) $_2$B boride has the strong chemical stability due to the B—B bond and the B—M (Fe, Cr) bond, a long incubation time is required to break these chemical bonds [22,38]. At the same time, the Al atoms and the Fe atoms interdiffuse to form the Fe-Al IMCs, and then the special PLS is formed in the IMC layer. Studies [22,23] have shown that PLSs can not only effectively inhibit the interdiffusion between the matrix and the Al melts, but also enhance the bonding between the matrix and the IMCs and the internal strength of the IMC layer, thereby hindering the exfoliation and dissolution of the corrosion layer. As shown in Fig. 9a, ceramic particles are dissociated from the matrix and distributed separately in the IMC and solidified aluminum layers, which can also cause the diffusion inhibition of Al atoms to some extent. In the solidified aluminum layer, a large quantity of elongated strip-shaped $FeAl_3$ and flocculent eutectics of $FeAl_3$ and Al are observed as well (Tables 4 and 5).

Table 4
Chemical compositions at the marked locations in Fig. 9a.

Location	Al	EDS results (wt.%)			
		Fe	Cr	B	Phase Compositions
1	58.69	33.32	7.99	–	$(Fe,Cr)Al_3$
2	55.95	20.69	14.42	8.94	$(Fe,Cr)_{0.8}Al_{2.5}B$
3	31.41	9.93	41.04	17.62	$(Cr,Fe)_{0.6}Al_{0.7}B$
4	65.85	27.43	6.72	–	Free $(Fe,Cr)Al_3$
5	61.15	0.47	20.80	17.58	$Cr_{0.25}Al_{1.4}B$

Table 5
Parameters for the model calculation.

Parameter	Unit	1023 K (750 °C)	Remark
W_{IMC}	*kg/mol*	2.47×10^{1}	This work
W_{Fe}	*kg/mol*	5.59×10^{2}	This work
$_{IMC}$	*kg/m*^{3}	4.0×10^{3}	[51]
$_{Fe}$	*kg/m*^{3}	7.86×10^{3}	[53]
C_{II}-C_I	*mol/m*^{3}	8×10^{3}	[54]
C_S	*mol/m*^{3}	1.07×10^{3}	[51]
ν	m^2/s	4.79×10^{7}	[51]
	r/min	60	This work
D	m^2/s	1.84×10^{8}	[55]

4. Discussion

4.1. Thermodynamic analysis of carbides and borides

After the addition of B and Ti elements, TiC, TiB_2, TiB, Fe_2B and FeB may be competitively precipitated during solidification. However, for the JDF alloys, only TiC, TiB_2 and Fe_2B phases exist in the as-cast microstructure. Studies have shown that the formation probability of various phases can be estimated via the Gibbs free energy (ΔG) of the IMCs, which is given by [41]

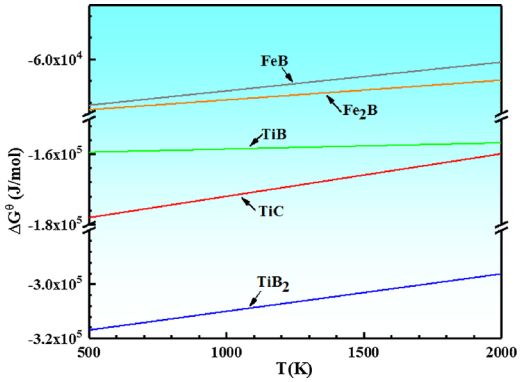

Fig. 10. Gibbs free energy of compounds as a function of temperature.

$$G = H_{298K} - T S_{298K} \quad (2)$$

where G is the Gibbs free energy of compounds under standard conditions, H_{298K} and S_{298K} are the changes in enthalpy and entropy of compounds under standard conditions, respectively, and T is the thermodynamic temperature. Some possible compounds formed in JDF alloys are listed in Eqs. (3)–(7):

$$Ti + C = TiC: \quad G_{TiC} = -184096 + 12.134T \quad (3)$$

$$Ti + B = TiB: \quad G_{TiB} = -160247 + 1.77T \quad (4)$$

$$Ti + 2B = TiB_2: \quad G_{TiB_2} = -323842 + 13.874T \quad (5)$$

$$Fe + B = FeB: \quad G_{FeB} = -71128 + 5.314T \quad (6)$$

$$Fe + 2B = FeB_2: \quad G_{FeB_2} = -71128 + 3.641T \quad (7)$$

The variations of the Gibbs free energy G of the reactions with the temperature are shown in Fig. 10. The reaction thermodynamics analysis suggests that the lower the standard Gibbs free energy, the more stable the compound. Therefore, the thermodynamically stable TiB_2 and TiC particles are preferentially formed when Ti and graphite are added to the melt. Furthermore, with decreasing the melt temperature, the solubility of carbides and borides in the steel decreases. When the actual solubility product of the carbide or boride is larger than the equilibrium solubility product, ceramic particles are precipitated in the molten steel [42]. Since the atomic percentage of Ti added is much lower than that of B, TiB_2 and TiC particles generated during solidification are mostly present in the form of nanoparticles or particles with several micrometers. The same phenomenon is also found in the earlier published papers [43–46].

4.2. Growth kinetics of the IMC layer

Studies [19,47,48] have shown that the high temperature erosion-corrosion process is not a simple combination of erosion and corrosion. Actually, it is a complicated dynamic process in which erosion and corrosion interact and influence each other, so that the corrosion of materials is accelerated. As illustrated in Fig. 11, ferrous alloy with multiscale compounds is corroded first by Al melts, followed by the interdiffusion between Fe and Al atoms at the solid/liquid interface (Fig. 11 a). After a period of time, a thin layer porous corrosion product composed of Fe-Al IMCs is formed preferentially. Since borides and ceramic particles have poor wettability with Al melts and react hardly with Al melts, the corrosion resistance of borides and ceramic particles is much superior to that of the ferrous matrix, which leads to the entrapment of some borides and ceramic particles in the Fe-Al IMC layer (Fig. 11b). Nevertheless, because of the dissolution of Fe in Cr-rich Fe_2B and the diffusion of Al atoms, Cr-rich Fe_2B can be corroded by the melt via the reaction: $(Cr,Fe)_2B + Al \rightarrow Cr\text{-}Al\text{-}B + Fe\text{-}Al$ [38–40]. As the erosion-corrosion process proceeds, the Fe-Al IMCs with the porous structure are inclined to be eroded and the borides embedded in the corrosion layer can also cause the microcrack initiation and propagation during the erosion of the Al melt, resulting in the fragmentation and exfoliation (Fig. 11c).

An analytical model, which is an extension of T-L-K model [49] to the situation of ferrous alloys with multiscale compounds, is established to describe the corrosion behavior of JDF alloys in the dynamic Al melts by making the assumptions: (1) Owing to the limited composition range of IMCs, the interdiffusion coefficient is considered to be independent of the composition. (2) The concentration gradient of Al in IMC layer is independent of the location. With corrosion time extending, the corrosion layer can be formed as shown in Fig. 11b. As Al atoms diffuse into the matrix through the IMC layer and react with the matrix, the interface between the matrix and the IMC layer (Interface I) migrates progressively towards the interior of the matrix, so that the thickness of the IMC layer is increased and the matrix is corroded. Simultaneously, because the dissolution of IMCs occurs continuously at the interface II near the Al melt, the interface II migrates gradually towards the matrix. Consequently, it can be assumed that the thickness (L) of IMC layer is mainly controlled by the growth and dissolution of IMCs.

The diffusion flux perpendicular to the interface is given by [50]:

$$J = -D\frac{dC}{dx} \quad (8)$$

where J is the diffusion flux of the Al atoms, C is the concentration of Al in the IMC layer, D is the interdiffusion coefficient of the IMCs, x is the location in the normal direction of diffusion, and minus sign (-) represents that the direction of the diffusion flow is opposite to that of the concentration gradient.

In the model, the concentration gradient of Al in the IMC layer is taken to be independent of location, thus

$$\frac{dC}{dx} = \frac{C_I - C_{II}}{L} \quad (9)$$

where C_I and C_{II} are the concentration of Al at the interface I and II, respectively. To clarify the extent to which the multiscale compounds can affect the diffusion of Al melts into the matrix, the diffusion inhibition factor is introduced. By substituting Eq. (9) into Eq. (8) and rearranging one has

$$J = -\frac{D(C_{II} - C_I)}{L} \quad (10)$$

During the corrosion of JDF alloys, if the thickness of newly-formed IMCs in a duration dt is defined as dL_g, then the relationship between dL_g and dt is given by

$$\int J S dt = \frac{b_{IMC} S dL_g}{W_{IMC}} = -\frac{D(C_{II} - C_I)}{L} S dt \quad (11)$$

where t is the corrosion time, b is the stoichiometric ratio of Al in the IMC ($Fe_a Al_b$), $_{IMC}$ is the density of the IMC, S is the contact area of IMCs with the Al melts, L_g is the thickness of the IMC, and W_{IMC} is the molar mass of the IMC. Therefore, the growth rate of the IMC can be calculated by

$$\frac{dL_g}{dt} = \frac{DW_{IMC}(C_{II} - C_I)}{b_{IMC} L} \quad (12)$$

At the interface II, the dissolution of IMCs into Al melts can be described by the Nernst- Shchukarev equation [51]:

$$\frac{dC}{dt} = K\frac{S}{V}(C_S - C) \quad (13)$$

where C is the concentration of Fe in the Al melt, K is the dissolution rate constant, V is the volume of the Al melt, and C_S is the saturation concentration of Fe in the Al melt. The corrosion of the IMC layer during the dynamic corrosion can affect the dissolution constant K [51,52].

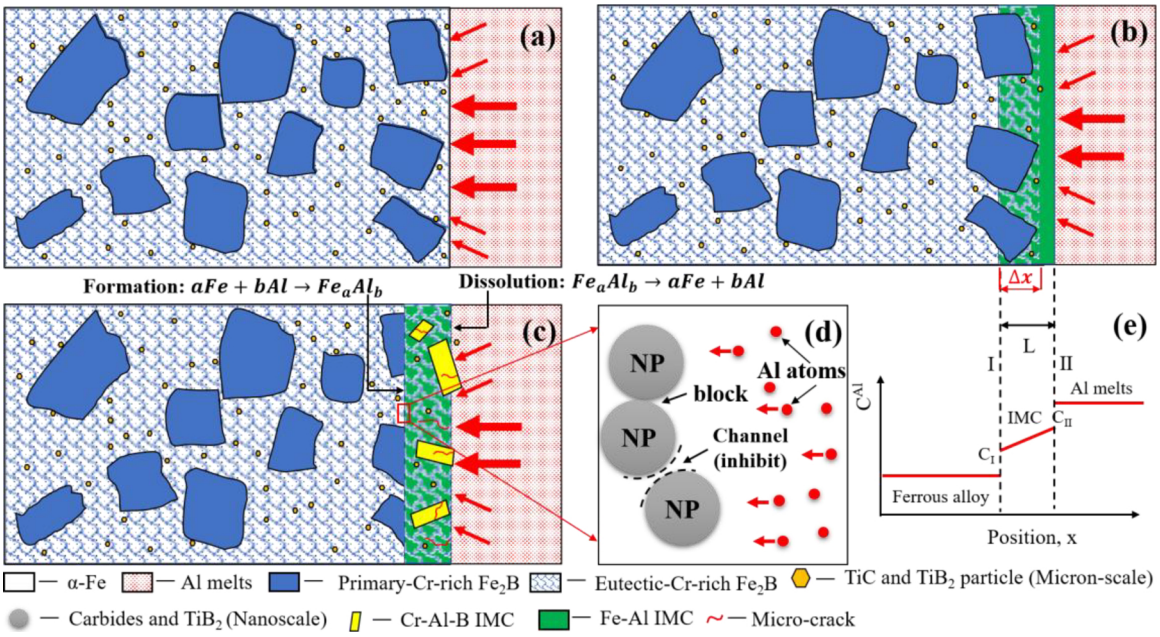

Fig. 11. The schematic of the erosion-corrosion mechanisms of the JDF alloys in Al melts.

$$K_d = 0.554 I \, {}^{1}D^{2/3} \nu^{1/6} \, {}^{1/2} \tag{14}$$

$$I\left(\frac{D}{\nu}\right) = \int_0^{1.9944(\nu/D)^{1/3}} \exp\left(X^3 + 0.885\left(\frac{D}{\nu}\right)^{1/3} X^4 \quad 0.394\left(\frac{D}{\nu}\right)^{2/3} X^5\right) dX \tag{15}$$

where ν is the kinematic viscosity of the melt, and is the angular speed of disc rotation.

During the time dt, the thickness dL_d of the IMC is decreased due to its dissolution, and the concentration of Fe in the Al melt is increased by dC, which can be given by

$$dC = \frac{{}_{IMC} S dL_d}{W_{IMC}} \frac{a}{V} \tag{16}$$

where a is the stoichiometric ratio of Fe in the IMC ($Fe_a Al_b$).

For an initial condition: $t = 0$ and $C = 0$,

$$C = C_S \left(1 \quad e^{\frac{K_d S}{V} t}\right) \tag{17}$$

The dissolution rate of the IMCs can be determined by

$$\frac{dL_d}{dt} = \frac{W_{IMC} V}{{}_{IMC} a S} K_d \frac{S}{V} (C_{II} \quad C_I) = \frac{C_S K_d W_{IMC}}{{}_{IMC} a} e^{\frac{K_d S}{V} t} \tag{18}$$

Taking into account that the volume V of the Al melt is large enough, the value of $S V^{-1}$ is nearly equal to 0, and thus

$$\frac{dL_d}{dt} = \frac{C_S K_d W_{IMC}}{{}_{IMC} a} \tag{19}$$

As the thickness of the IMC layer is controlled by its growth and dissolution, the variation rate of the IMC layer thickness is given by

$$\frac{dL}{dt} = \frac{dL_g}{dt} \quad \frac{dL_d}{dt} = \frac{D W_{IMC} (C_{II} \quad C_I)}{b \, {}_{IMC} L} \quad \frac{C_S K_d W_{IMC}}{{}_{IMC} a} \tag{20}$$

When $\frac{dL}{dt} = 0$, the growth and dissolution of IMCs reach a mutual equilibrium. As a result,

$$L_{max} = \frac{D (C_{II} \quad C_I) a}{C_S K_d b} \tag{21}$$

where L_{max} is the maximum thickness of the IMC layer.

In this model, the corrosion of JDF alloys is accompanied by the growth of IMCs. At the time of dt, the thickness of the IMC layer is increased by dL_g, and the corrosion rate of the matrix $d(\ x)/dt$ can be obtained as

$$\frac{d(\ x)}{dt} = \frac{a \, {}_{IMC} W_{Fe}}{{}_{Fe} W_{IMC}} \frac{dL_g}{dt} = \frac{a W_{Fe} D (C_{II} \quad C_I)}{b \, {}_{Fe} L} \tag{22}$$

where ${}_{Fe}$ and W_{Fe} are the density and molar of Fe, respectively. When the corrosion of JDF alloys is initiated, the thickness of the IMC layer is so small that $\frac{dL_g}{dt}$ $\frac{dL_d}{dt}$. Thus,

$$\frac{dL}{dt} = \frac{dL_g}{dt} \quad \frac{dL_d}{dt} \quad \frac{dL_g}{dt} \tag{23}$$

For an initial condition: $t = 0$ and $L = 0$,

$$L = \sqrt{\frac{2 W_{IMC} D (C_{II} \quad C_I)}{b \, {}_{IMC}}} \sqrt{t} \tag{24}$$

Then

$$\frac{d(\ x)}{dt} = \frac{a W_{Fe}}{{}_{Fe}} \sqrt{\frac{{}_{IMC} D (C_{II} \quad C_I)}{2 b W_{IMC}}} \frac{1}{\sqrt{t}} \tag{25}$$

$$x = \frac{a W_{Fe}}{{}_{Fe}} \sqrt{\frac{2 \, {}_{IMC} D (C_{II} \quad C_I)}{b W_{IMC}}} \sqrt{t} \tag{26}$$

Let

$$= \frac{a W_{Fe}}{{}_{Fe}} \sqrt{\frac{2 \, {}_{IMC} D (C_{II} \quad C_I)}{b W_{IMC}}} \tag{27}$$

Then

$$= \frac{2 \, {}_{IMC} D (C_{II} \quad C_I) a^2 W_{Fe}^2}{b W_{IMC} \, {}^2 \, {}^2_{Fe}} \tag{28}$$

The dependency of the thickness loss of ferrous alloys on the erosion-corrosion time is plotted in Fig. 12a, where the experimental, prediction and fitting results are compared. It is notable that the pure ferrous matrix has the largest x for which no diffusion inhibitor is considered, while JDF3 the minimum in which the multiscale compounds act as the strongest diffusion inhibitor. The diffusion inhibition factor ε is

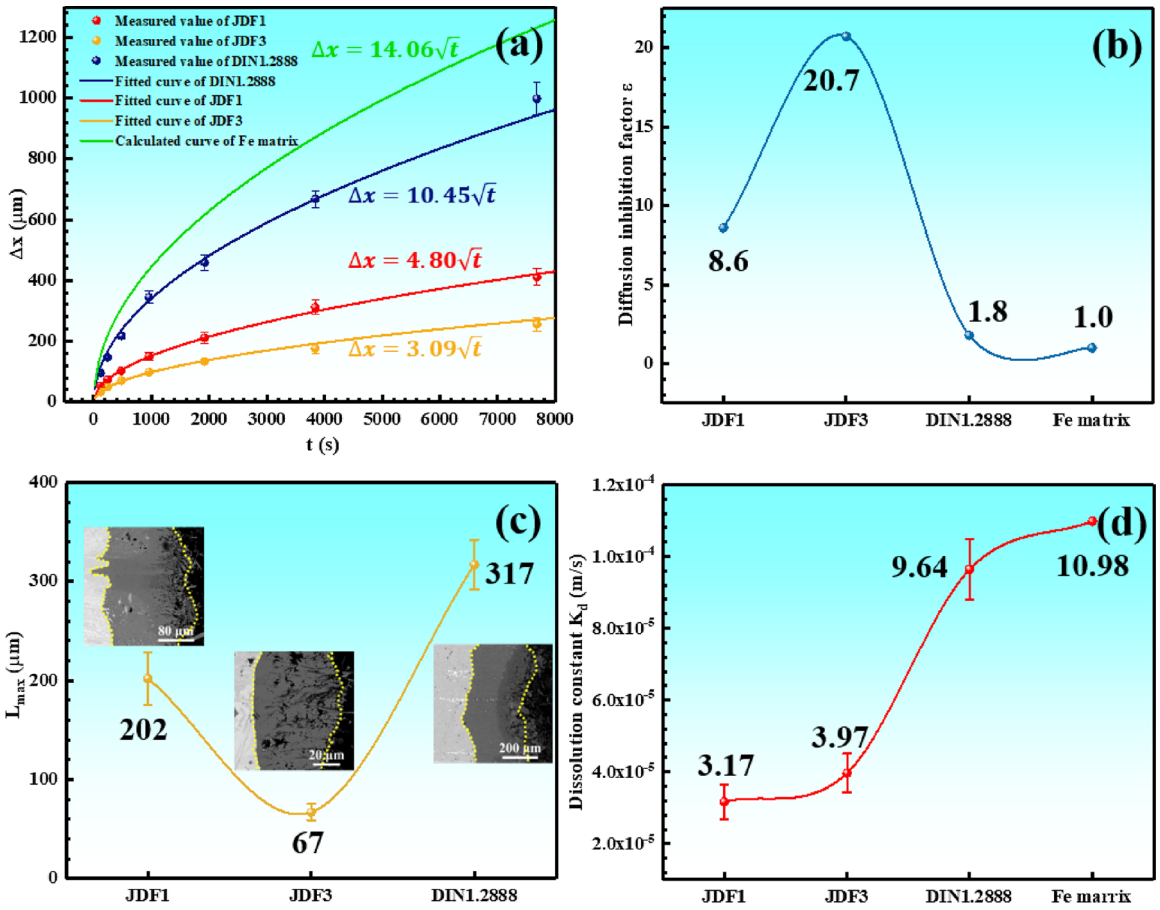

Fig. 12. (a) Matrix thickness loss of ferrous alloys vs erosion-corrosion time; (b) ε values for ferrous alloys; (c) maximum thickness of IMC layers in ferrous alloys; (d) K_d value for ferrous alloys; The insets in Fig. 12c are the SEM micrographs of the IMC layers in various ferrous alloys.

introduced to quantitatively describe the contribution of multiscale compounds to the diffusion inhibition and thereby the growth restriction of IMCs. For the pure ferrous matrix, the ε value is equal to 1. The values can be obtained from the fitted curves in Fig. 12a, and the ε values can be achieved by substituting the obtained values into Eq. (28). It is clear from Fig. 12b that JDF3 alloy has the maximum ε, meaning the strongest diffusion inhibition effect, which is in agreement with the experimental results in Fig. 7. Essentially, the diffusion inhibition factor ε reflects the corrosion resistance of alloys to the Al melts. The larger is ε, the higher the corrosion resistance of the alloy. The comparison of L_{max} for the three ferrous alloys is shown in Fig. 12c. DIN1.2888 alloy exhibits the largest L_{max}, whereas JDF3 alloy the smallest one. The corresponding K_d values can be attained by substituting the measured L_{max} and calculated ε of the three ferrous alloys into Eq. (21), and the K_d of the ferrous matrix as a reference is also obtained using Eq. (14). The calculation results indicate that the ferrous matrix has the largest K_d, followed by DIN1.2888, JDF3 and JDF1. The small K_d signifies the small quantity of dissolved corrosion products and the desirable corrosion resistance.

The experimental results and model analysis demonstrate that JDF alloys have the large ε and the low K_d during the dynamic Al melt corrosion, and the corrosion resistance of the JDF3 alloy is particularly prominent. The microstructure of the JDF3 alloy shows that it is a ferrous alloy containing multiscale compounds whose sizes range from micron to nano scale. The micron-scale compounds include the primary Cr-rich Fe_2B with tens of micrometers, the eutectic Cr-rich Fe_2B with several micrometers to several tens of micrometers, TiC and TiB_2 ceramic particles with 3 to 5 μms, and the nanoscale counterparts the carbide with hundreds of nanometers and TiB_2 nanoparticles with ten nanometers. The NPs that assemble onto the phase interface of borides are capable of restricting the growth of borides and refining the borides, increasing the number density of borides in the matrix and the contact area between borides and Al atoms, whereas those that are uniformly distributed in the matrix can effectively inhibit the diffusion of Al atoms into the matrix. Specifically, during the diffusion of the Al atoms into the matrix, many NPs distributed uniformly in the matrix are either adherent to each other or packed together forming channels between them. As shown in Fig. 11 d, the conjunction of NPs can completely block the diffusion of Al atoms into the matrix, while the channels between the particles can effectively limit the diffusion path of Al atoms, thus greatly inhibiting the diffusion process of Al atoms. The synergistic effect of these compounds ultimately leads to the enhanced multiscale corrosion resistance. In this work, ε is used as the quantitative indicator of this effect, and the JDF3 alloy has much larger ε than DIN 1.2888. By observing the corrosion interface of JDF alloys in the Al melts, it was found that the borides with the skeleton structure and the PLSs embedded in the corrosion layer can effectively improve the bonding strength between the matrix and the IMCs and the internal strength of the IMCs, which helps to hinder the exfoliation and dissolution of corrosion products. Hence, the JDF alloys have much smaller K_d than DIN 1.2888.

5. Conclusion

In this study, the interface morphology and erosion-corrosion behavior of JDF alloys in dynamic Al melts is investigated systematically. Combined with theoretical model analysis, the main conclusions could be summarized as follows:

(1) The JDF alloys exhibit outstanding corrosion resistance in the dynamic Al melts. Among them, the corrosion resistance of the JDF3

alloy is 2 times higher than that of FeCrB base alloy and almost 4 times higher than that of DIN1.2888.

(2) The JDF3 alloy with multiscale compounds can effectively inhibit the diffusion of Al melts in multiscales. The PLSs and borides with skeleton structure embedded in the Fe-Al IMC layer can play a critical role in hindering the exfoliation and dissolution of the corrosion products.

(3) The quantitative relationship between the thickness loss of the ferrous alloys and the diffusion inhibition factor ε is established and given by $x = \frac{aw_{Fe}}{Fe}\sqrt{\frac{2_{IMC}D(C_{II} \quad C_I)}{bw_{IMC}}}\sqrt{t}$.

(4) Essentially, the diffusion inhibition factor ε reflects the corrosion resistance of alloys to the Al melt. The higher is ε, the stronger the corrosion resistance of the alloys.

Data availability statement

All data included in this study are available upon request by contact with the corresponding author.

Declaration of Competing Interest

We declare that we do not have any commercial or associative interest that represents a conflict of interest in connection with the work submitted.

Acknowledgement

The present study was sponsored by the National Natural Science Foundation of China, People's Republic of China (NSFC) under Grant no. 51804197. Startup Fund for Youngman Research at SJTU (SFYR at SJTU).

References

[1] K.A. Nazari, S.G. Shabestari, Effect of micro alloying elements on the interfacial reactions between molten aluminum alloy and tool steel, J. Alloys Compd. 478 (2009) 523–530.
[2] J.H. Kim, S.Y. Kim, C.Y. Kang, Effect of phase difference on growth kinetic of alloy layer in aluminized and diffusion-treated 12% Cr heating resistant steels, Surf. Coat. Technol. 240 (2014) 387–392.
[3] G.H. Awan, F.U. Hasan, The morphology of coating/substrate interface in hot-dip-aluminized steels, Mater. Sci. Eng. A 472 (2008) 157–165.
[4] X.X. Hou, H. Yang, Y. Zhao, F.Z. Pan, Effect of Si on the interaction between die casting die and aluminum alloy, Mater. Lett. 58 (2004) 3424–3427.
[5] A.E. Miller, D.M. Maijer, Investigation of erosive-corrosive wear in the low pressure die casting of aluminum A356, Mater. Sci. Eng. A 435 (2006) 100–111.
[6] D. Wang, Z. Shi, L. Zou, A liquid aluminum corrosion resistance surface on steel substrate, Appl. Surf. Sci. 214 (2003) 304–311.
[7] D. Balloy, J.C. Tissier, M.L. Giorgi, M. Briant, Corrosion mechanisms of steel and cast iron by molten aluminum, Metall. Mater. Trans. A 41 (2010) 2366–2376.
[8] N. Tunca, G.W. Delamore, R.W. Smith, Corrosion of Mo, Nb, Cr, and Y in molten aluminum, Metall. Mater. Trans. A 21 (1990) 2919–2928.
[9] Y. Li, N. Tang, P. Tunthawiroon, Y. Koizumi, A. chiba, Characterisation of oxide films formed on Co–29Cr–6Mo alloy used in die-casting moulds for aluminium, Corros. Sci. 73 (2013) 72–79.
[10] X.M. Zhang, W.P. Chen, Review on corrosion-wear resistance performance of materials in molten aluminum and its alloys, Trans. Nonferrous Met. Soc. China 25 (2015) 1715–1731.
[11] M. Tanaka, K. Kashiwagi, N. Kawashima, S. Kitaoka, O. Sakurada, Y. Ohya, Effect of grain boundary cracks on the corrosion behaviour of aluminium titanate ceramics in a molten aluminium alloy, Corros. Sci. 54 (2012) 90–96.
[12] S.Q. Ma, J.D. Xing, Y.L. He, H.G. Fu, Y.F. Li, G.Z. Liu, Effect of orientation and lamellar spacing of Fe2B on interfaces and corrosion behavior of Fe-B alloy in hot-dip galvanization, Acta Mater. 115 (2016) 392–402.
[13] S.Q. Ma, J.D. Xing, H.G. Fu, Y.L. He, Y. Bai, Y.F. Li, Y.P. Bai, Interface characteristics and corrosion behavior of oriented bulk Fe2B alloy in liquid zinc, Corros. Sci. 78 (2014) 71–80.
[14] Y. Wang, J. Xing, S. Ma, G. Liu, S. Jia, Erosion–corrosion interaction of Fe–B alloy in flowing zinc, Mater. Sci. Technol. 32 (2016) 49–56.
[15] Y. Wang, J.D. Xing, S.Q. Ma, B.C. Zheng, H.G. Fu, G.Z. Liu, Interfacial morphologies and erosion–corrosion behavior of directional Fe-3.5 wt.% B steel in flowing liquid Zn containing 0.30 wt.% Al, Corros. Sci. 112 (2016) 25–35.
[16] S.Q. Ma, J.D. Xing, D.W. Yi, H.G. Fu, G.F. Liu, S.C. Ma, Microstructure and corrosion behavior of cast Fe–B alloys dipped into liquid zinc bath, Mater. Charact. 61 (2010) 866–872.
[17] X. Liu, M.M. Wang, F.C. Yin, X.M. Ouyang, Z. Li, Effects of Tungsten Addition on the Microstructure and Corrosion Resistance of Fe-3.5 B Alloy in Liquid Zinc, Mater. 10 (2017) 399.
[18] M.M. Wang, J. Xue, R. Gao, H.Y. Gao, Y. Zhou, Y.Y. Zhao, Y.H. Liu, M.D. Kang, J. Wang, Interface morphology and corrosion behavior of bulk Fe_2B in liquid Al, Mater. Charact. 152 (2019) 1–11.
[19] Y. Wang, J.D. Xing, H.G. Fu, Y.Z. Liu, K.H. Zheng, S.Q. Ma, Y.X. Jian, Interfacial morphology and corrosion-wear behavior of cast Fe-3.5 wt.% B steel in liquid zinc, Corros. Sci. 131 (2018) 290–299.
[20] S.Q. Ma, J.D. Xing, H.G. Fu, D.W. Yi, X.H. Zhi, Y.F. Li, Effects of boron concentration on the corrosion resistance of Fe–B alloys immersed in 460 C molten zinc bath, Surf. Coat. Technol. 204 (2010) 2208–2214.
[21] X.M. Zhang, W.P. Chen, H.F. Luo, S. Li, T. Zhou, L.Y. Shi, Corrosion resistance and interfacial morphologies of novel Fe-Cr-Mo-B cast steels in molten aluminum, Corros. Sci. 125 (2017) 20–28.
[22] Z.C. Ling, W.P. Chen, T.W. Lu, B. Li, X.M. Zhang, Interfacial morphology and tribo-corrosion behaviour of Fe-15.3 wt% Cr-3.1 wt% B-6.2 wt% Mo alloy in molten aluminium, Wear 430 (2019) 81–93.
[23] Z.C. Ling, W.P. Chen, W.Y. Xu, X.M. Zhang, T.W. Lu, J. Liu, The influence of A Mo addition on the interfacial morphologies and corrosion resistances of novel Fe-Cr-B alloys immersed in molten aluminum, Materials 12 (2019) 256.
[24] X.M. Zhang, W.P. Chen, H.F. Luo, Corrosion-Wear Resistance and Interfacial Morphologies of Novel Fe–Cr–B Cast Steels in Molten Aluminum, Tribol. Lett. 66 (2018) 112.
[25] S.Q. Ma, J.D. Xing, G.F. Liu, D.W. Yi, H.G. Fu, J.J. Zhang, Y.F. Li, Effect of chromium concentration on microstructure and properties of Fe-3.5 B alloy, Mater. Sci. Eng. A 527 (2010) 6800–6808.
[26] J.J. Zhang, Y.M. Gao, J.D. Xing, S.Q. Ma, D.W. Yi, J.B. Yan, Effects of chromium addition on microstructure and abrasion resistance of Fe–B cast alloy, Tribol. Lett. 44 (2011) 31.
[27] Y.X. Jian, Z.F. Huang, J.D. Xing, Y.M. Gao, Effects of chromium on the morphology and mechanical properties of Fe_2B intermetallic in Fe-3.0B alloy, J. Mater. Sci. 53 (2018) 5329–5338.
[28] B.H. Li, Y. Liu, J. Li, L. He, Effect of sintering process on the microstructures and properties of in situ TiB_2–TiC reinforced steel matrix composites produced by spark plasma sintering, J. Mater. Process. Technol. 210 (2010) 91–95.
[29] Y.F. Yang, Q.C. Jiang, Effect of TiB_2/TiC ratio on the microstructure and mechanical properties of high volume fractions of TiB_2/TiC reinforced Fe matrix composite, Int. J. Refract. Met. Hard Mater. 38 (2013) 137–139.
[30] K. Wang, H.Y. Jiang, Y.W. Jia, H. Zhou, Q.D. Wang, B. Ye, W.J. Ding, Nanoparticle-inhibited growth of primary aluminum in Al-10Si alloys, Acta Mater. 103 (2016) 252–263.
[31] K. Wang, H.Y. Jiang, Q.D. Wang, B. Ye, W.J. Ding, A novel method to achieve grain refinement in aluminum, Metall. Mater. Trans. A 47 (2016) 4788–4794.
[32] K. Wang, H.Y. Jiang, Y.X. Wang, Q.D. Wang, B. Ye, W.J. Ding, Microstructure and mechanical properties of hypoeutectic Al-Si composite reinforced with TiCN nanoparticles, Mater. Des. 95 (2016) 545–554.
[33] N. Tang, Y.P. Li, S. Kurosu, H. Matsumoto, A. Chiba, Interfacial reactions of solid Co and solid Fe with liquid Al, Corros. Sci. 60 (2012) 32–37.
[34] S. Chen, D. Yang, M. Zhang, J. Huang, X. Zhao, Interaction between the growth and dissolution of intermetallic compounds in the interfacial reaction between solid iron and liquid aluminum, Metall. Mater. Trans. A 47 (2016) 5088–5100.
[35] H. Xiao, W. Chen, Z. Liu, Corrosion resistance of 91W–6Ni–3Fe refractory metal, TiAl compound and iron based alloys in liquid aluminum, Trans. Nonferrous Met. Soc. China 22 (2012) 2320–2326.
[36] T. Heumann, S. Dittrich, Uber die Kinetik der Reaktion von festem und flûssigem aluminium mit Eisen, Z. Metallkunde 50 (1959) 617–625.
[37] N.L. Okamoto, J. Okumura, M. Higashi, H. Inui, Crystal structure of η′-Fe3Al8; low-temperature phase of η-Fe2Al5 accompanied by an ordered arrangement of Al atoms of full occupancy in the c-axis chain sites, Acta Mater. 129 (2017) 290–299.
[38] X.M. Zhang, W.P. Chen, H.F. Luo, T. Zhou, Formation of periodic layered structure between novel Fe-Cr-B cast steel and molten aluminum, Scr. Mater. 130 (2017) 288–291.
[39] X.M. Zhang, W.P. Chen, H.F. Luo, Z.C. Ling, J. Wang, T. Zhou, S. Li, Influence of Cr on the interfacial boride reaction between Fe-Cr-B cast steel and molten aluminium, Corros. Sci. 158 (2019) 108098.
[40] Z.C. Ling, W.P. Chen, X. Yang, B. Li, T.W. Lu, Interfacial morphologies and corrosion behaviours of novel Fe-Cr-B alloys immersed in molten aluminium, Mater. Res. Express 6 (2019) 046557.
[41] D.L. Ye, J.H. Hu, Practical Handbook of Thermodynamic Data for Inorganic Compounds, 2nd ed., Metallurgical Industry Press, Beijing, 2002, p. 1.
[42] T. Gladman, Precipitation hardening in metals, Mater. Sci. Technol. 15 (1999) 30–36.
[43] Y.E. Gol'dshtein, V.G. Mizin, Some peculiarities of the structure of high boron steels, Met. Sci. Heat Treat. 30 (1988) 479–484.
[44] H. Springer, R.A. Fernandez, M.J. Duarte, A. Kostka, D. Raabe, Microstructure refinement for high modulus in-situ metal matrix composite steels via controlled solidification of the system Fe–TiB2, Acta Mater. 96 (2015) 47–56.
[45] H. Fu, Q. Xiao, J. Kuang, Z. Jiang, J. Xing, Effect of rare earth and titanium additions on the microstructures and properties of low carbon Fe–B cast steel, Mater. Sci. and Eng. A 466 (2007) 160–165.
[46] L. Cha, S. Lartigue-Korinek, M. Walls, L. Mazerolles, Interface structure and chemistry in a novel steel-based composite Fe–TiB2 obtained by eutectic solidification, Acta Mater. 60 (2012) 6382–6389.
[47] G.Z. Liu, S.Q. Ma, J.D. Xing, H.G. Fu, Y. Gao, Y.P. Bai, Y. Wang, Investigation of

flowing liquid zinc erosion and corrosion properties of the Fe–B alloy at various times, J. Mater. Res. 30 (2015) 727–735.
[48] Y. Wang, J.D. Xing, S.Q. Ma, G.Z. Liu, S. Jia, Erosion–corrosion interaction of Fe–B alloy in flowing zinc, Mater. Sci. Technol. 32 (2016) 49–56.
[49] N. Tang, Y. Li, Y. Koizumi, S. Kurosu, A. Chiba, Experimental and theoretical research on interfacial reaction of solid Co with liquid Al, Corros. Sci. 73 (2013) 54–61.
[50] L.L. Bircumshaw, A.C. Riddiford, Transport control in heterogeneous reactions, Q. Rev. Chem. Soc. 6 (1952) 157–185.
[51] V.N. Yeremenko, Y.V. Natanzon, V.I. Dybkov, The effect of dissolution on the growth of the Fe2Al5 interlayer in the solid iron-liquid aluminium system, J. Mater. Sci. 16 (1981) 1748–1756.
[52] T.F. Kassner, Rate of solution of rotating tantalum disks in liquid tin, J. Electrochem. Soc. 114 (1967) 689–694.
[53] J.R. Davis, ASM Metal Handbook: Desk Edition, ASM International, OH, USA, 1998.
[54] H. Baker, Okamoto H, ASM handbook: alloy phase diagrams, ASM International, OH, USA, 1992.
[55] K. Bouche, F. Barbier, A. Coulet, Intermetallic compound layer growth between solid iron and molten aluminium, Mater. Sci. Eng. A 249 (1998) 167–175.